Nanoscale Advances

ROYAL SOCIETY OF CHEMISTRY

PAPER

View Article Online
View Journal | View Issue

Cite this: *Nanoscale Adv.*, 2026, **8**, 565

Facile two-step synthesis of yttrium-doped g-C_3N_4 for enhanced photocatalytic degradation of methylene blue with self-cleaning properties

Muhammad Ikram Nabeel,[a] Naseer Ahmad,[a] Shan Arif,[a] Dilshad Hussain *[a] and Syed Ghulam Musharraf *[ab]

In this study, porous graphitic carbon nitride (g-C_3N_4) with different yttrium (Y) doping ratios are synthesized using a facile two-step pyrolysis method, yielding Y/g-C_3N_4-1, Y/g-C_3N_4-2, Y/g-C_3N_4-3, and Y/g-C_3N_4-4. These synthesized materials are used for the photocatalytic degradation of methylene blue (MB). Among the synthesized combinations, Y/g-C_3N_4-3 showed the highest photocatalytic activity (99%) under visible light. It exhibited pseudo-first-order kinetic behavior (k = 0.0439 min^{-1}, R^2 = 0.999, $t_{1/2}$ = 15.78 min) for MB degradation, outperforming the other materials. In tap water, Y/g-C_3N_4-3 achieved a 90% degradation efficiency for the target dye. The total organic carbon (TOC) removal reached 87%, further reinforcing its effectiveness. Electrochemical impedance spectroscopy (EIS) was performed, where a smaller semicircle for Y/g-C_3N_4-3 indicated lower charge transfer resistance and improved carrier mobility. To identify reactive species, a radical scavenger experiment was performed, revealing holes (h^+) as the primary reactive species, while $^{\bullet}OH$, e^-, and $^{\bullet}O_2^-$ played a minor role in MB degradation. The optimized photocatalyst was coated on the fabric surface using the drop-casting method to evaluate its self-cleaning properties. This work highlights the promising potential of rare earth metal doping as a versatile strategy for synthesizing high-performance g-C_3N_4-based photocatalysts.

Received 18th June 2025
Accepted 28th October 2025

DOI: 10.1039/d5na00600g

rsc.li/nanoscale-advances

1 Introduction

Rapid industrial growth has directly contributed to water pollution,[1] a major global concern that has been a pressing issue for the past decade.[2,3] Many types of water contaminants, including drugs, dyes, pesticides, and oils, are directly discharged into water streams. Organic dyes are widely used in cosmetics, textiles, food processing, plastics, and paper manufacturing.[4,5] Nearly 15% of global dye production is lost during the dyeing process and released into water reservoirs.[6,7] These dyes, as persistent organic pollutants, pose a significant threat to water quality.[8,9] Methylene blue (MB) is one of the widely used dyes in the textile industry, as well as in biological and chemical fields, which significantly contributes to environmental pollution.[10,11] MB disrupts aquatic ecosystems by reducing oxygen levels, accumulating in organisms, and hindering photosynthesis. In humans, it causes neurotoxicity, allergies, methemoglobinemia, and digestive issues.[12] Therefore, it is necessary to remove it using suitable methods.

Numerous techniques have been employed for MB removal, including ozonation, adsorption, chlorination, coagulation, membrane filtration, biological treatment, electrochemical processes, and advanced oxidation processes (AOPs).[13–16] Photocatalysis as an AOP which can effectively degrade MB, offering a fast, efficient, cost-effective, and eco-friendly solution.[17] Conventionally, semiconductor materials are used as photocatalysts, which generate electron–hole pairs (e^-/h^+) when irradiated with light. These e^-/h^+ produce reactive oxygen species (ROS) after interaction with water molecules ($^{\bullet}OH$, $O_2^{\bullet-}$, and H_2O_2), which degrade MB into H_2O and CO_2. Many semiconductors, including CdS, SnO_2, TiO_2, ZnO, CeO_2, WOx, Fe_2O_3, ZnS, g-C_3N_4, GO, and MXene, have been tested as photocatalysts for MB degradation.[13,18–22]

Among them, g-C_3N_4 is a promising photocatalyst due to its facile preparation, thermal stability, tailorable microstructure, good stability, and a suitable bandgap (~2.7–3.0 eV) for light absorption.[13,23] However, g-C_3N_4 exhibits a high electron–hole pair recombination rate, low electrical conductivity, a small specific surface area, and a low quantum efficiency.[24,25] Previously, various strategies, including metal/non-metal doping, heterojunction formation, and surface modification of g-C_3N_4, have been employed to enhance its photocatalytic efficiency. Metal doping, including noble metals (Ag, Pd, and Au) and transition metals (Zr, Ti, V, Y, and Zn) effectively eliminates this limitation.[5,26,27] Metal doping in g-C_3N_4 also produces metal–

[a]*HEJ Research Institute of Chemistry, International Center for Chemical and Biological Sciences, University of Karachi, Karachi 75270, Pakistan. E-mail: dilshadhussain@iccs.edu; musharraf1977@yahoo.com*

[b]*Panjwani Center for Molecular Medicines and Drug Research, International Center for Chemical and Biological Sciences, University of Karachi, Karachi, 75270, Pakistan*

semiconductor heterojunctions (Schottky barrier or ohmic contact), which further facilitate e^-/h^+ separation and enhance photocatalytic performance. However, the doping of transition metals is often hindered by instability and recombination, while the high cost of noble metals impedes their practical scalability.

Currently, doping with rare earth metals has received considerable attention in photocatalysis due to their f-orbital electronic properties. Yttrium (Y) is a particularly suitable element for doping since it acts as an efficient electron mediator for increased superoxide radical formation and charge separation. Its stable oxidation state (Y^{3+}) decreases photo-corrosion, which results in the long-term utilization of the photocatalyst. Furthermore, Y-doping alters the surface chemistry, introducing Lewis acid sites that enhance adsorption and provide a basis for utilizing photon conversion to extend the visible light absorption range. It also offers a versatile enhancement strategy that addresses the key limitations of g-C_3N_4 better than many transition and noble metal doping.[28–31]

Here, a highly efficient Y/g-C_3N_4 photocatalyst is synthesized by a two-step pyrolysis method for the visible-light-driven photocatalytic degradation of MB. This approach provides enhanced control over structural and surface properties, leading to improved porosity, increased surface area, and superior photocatalytic efficiency. Different combinations of photocatalysts are prepared by using different doping ratios. The degradation pathway of MB is elucidated based on the intermediate products identified through LC-MS analysis. The most effective catalyst is then coated onto fabric to evaluate its photocatalytic self-cleaning performance.

2 Experimental

2.1. Synthesis method

For this study, analytical-grade urea and yttrium nitrate hexahydrate were used without any purification. Pristine and Y-doped g-C_3N_4 materials were prepared using a two-step pyrolysis method (Scheme 1). 10 g of urea was dissolved in 20 mL of deionized water under magnetic stirring and then poured into a Petri dish for 1 day for water evaporation. The material was dried overnight in an oven at 80 °C. Finally, the dry powder was collected in a crucible and heated at 390 °C for 2 h, resulting in the formation of dark yellow precipitates, which were then cooled to room temperature. The product was again calcined at

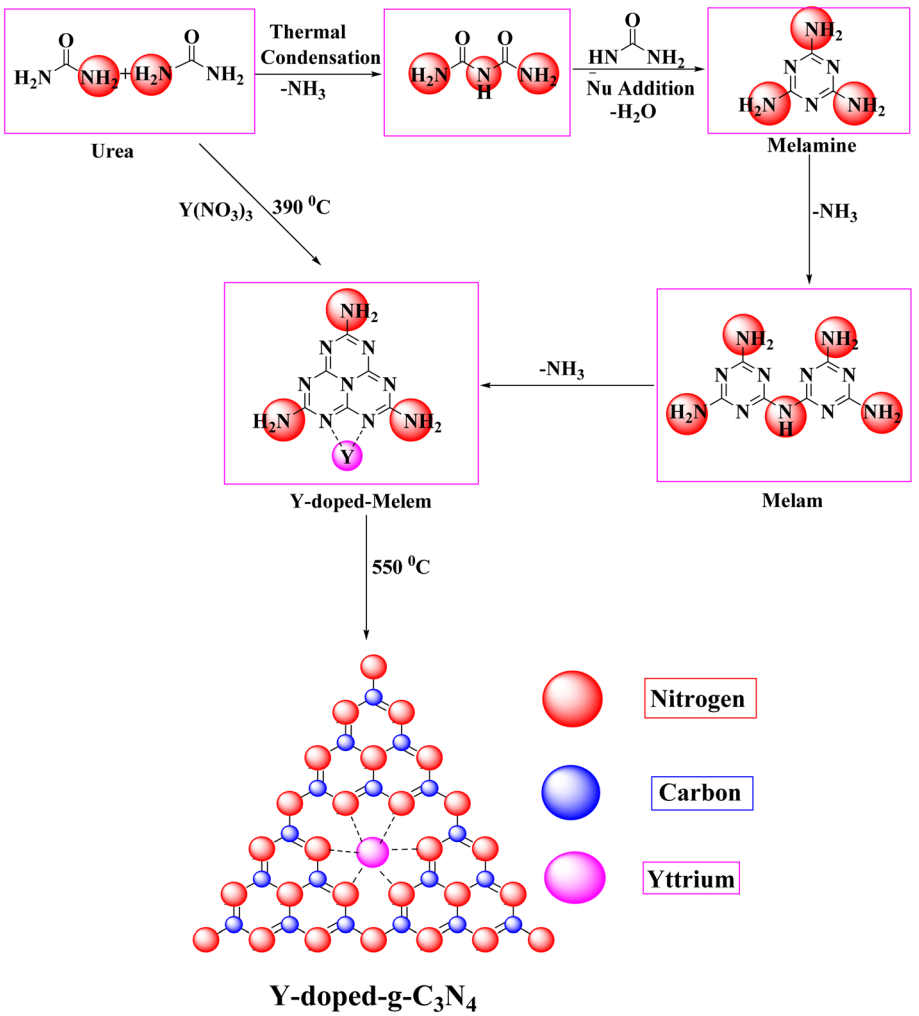

Scheme 1 Two-step pyrolysis method for the preparation of pure and Y/g-C_3N_4.

550 °C for 2.5 h in a muffle furnace at a ramp rate of 15 °C min^{-1}. After calcination, a light yellowish material was obtained, which was marked as g-C_3N_4. The same method was used to prepare Y/g-C_3N_4. *X* amount of Y-precursor was dissolved in 20 mL of deionized water. After a few minutes, 10 g urea was added, and the same procedure was repeated as described above. According to different mmol ratio-*x* (0.1, 0.25, 0.5, 1.0) of the Y-precursor, a different combination of Y/g-C_3N_4 was synthesized (Y/g-C_3N_4-1, Y/g-C_3N_4-2, Y/g-C_3N_4-3, and Y/g-C_3N_4-4).

2.2. Characterization of photocatalyst

Functional groups and crystal structures of synthesized materials were analyzed by Fourier transform infrared spectroscopy (FT-IR Thermo Scientific Nicolet) and X-ray diffraction (XRD D8 Advance X-ray Diffractometer). The surface area, pore volume, pore size, and thermal stability of materials were examined using Brunauer–Emmett–Teller (Nova 1000 Analyzer), thermogravimetric (TGA-PerkinElmer), and differential scanning calorimetry (DSC) analyses. The changes in optical properties were confirmed by UV-visible spectroscopy (Thermo Fisher Scientific, Evolution-201) and photoluminescence (PL) analysis. The morphology, structural features, and chemical composition of prepared materials were characterized using energy-dispersive X-ray spectroscopy (EDX), atomic force microscopy (AFM; Agilent 5500), and scanning electron microscopy (SEM; Thermo Fisher Apreo 2C LoVac). The particle size and surface charge of the photocatalysts were measured using a Malvern Nano Zetasizer. Zeta potential was determined using a Zeta Dip Cell under standard measurement conditions. For each measurement, the photocatalytic material (1 mg) was diluted in 5 mL MilliQ water (resistivity 18.2 MΩ cm), sonicated for 10 minutes, and then filtered with a 0.2 μm filter.

2.3. Photocatalytic tests

Photocatalytic activities of pure and Y/g-C_3N_4 were tested under a 400 W xenon lamp (visible range: 400 nm to 800 nm) for MB. 30 mg of the material was mixed with 50 mL of MB aqueous solution (MB concentration: 10 mg L^{-1}). Before starting the experiment, the mixed solution was stirred in the dark for 20 minutes until the photocatalyst and MB solution achieved the adsorption/desorption equilibrium. After that, the solution was placed under visible light, and a small amount (2 mL) of the dye was taken out for UV analysis every 5 minutes. The same experiment was also repeated without using the photocatalyst to check the stability of MB under visible light. The photocatalytic degradation efficiency was measured by using eqn (1):

$$\text{Degradation (\%)} = (C_0 - C_t)/C_0 \times 100\% \quad (1)$$

where C_0 is the original absorbance and C_t absorbance after 5 minutes.

2.4. LC-MS analysis of MB degradation products

The mass-to-charge ratio (*m*/*z*) of MB-degraded products was analyzed using a liquid chromatography-tandem mass spectrometer (LC-MS) equipped with an autosampler (Thermo Fisher Dionex UltiMate 3000 HPLC coupled with a Bruker Daltonics MaXis II ESI-QTOF-MS instrument, Bremen). A reverse-phase ELIPSE C-18 column (2.0 mm × 100 mm, 1.8 mm) with a guard column (2.0 mm × 4 mm, 1.8 mm) was used for the analysis. An LC-MS system equipped with an electrospray ionization (ESI) source was used to identify intermediates under the following conditions: capillary voltage 4500 (V), end plate offset 500 V, nebulizer gas 2.8 bar, drying gas flow (N_2) 6 L min^{-1}, temperature 200 °C, scan speed 5 Hz (MS) and 12 Hz (MS/MS), mass range 50–400*m*/*z*. The mobile phase was composed of a 40 : 60 ratio of ethanol and water, eluted under isocratic conditions, and filtered through a 0.2 μm filter. The flow rate was 1.0 mL min^{-1}, and the injection volume was 2.0 μL.

2.4.1. Identification of reactive oxygen species (ROS). To identify the ROS, such as $^{\bullet}OH$, h^+, $^1O_2$, and $^{\bullet}O_2^-$, quenching analysis was performed using different types of scavengers. Isopropyl alcohol (IPA, 10 mM), benzoquinone (BQ, 0.5 μM), ethylenediamine tetraacetic acid (EDTA, 0.20 mol L^{-1}), and sodium azide (0.5 μM) were used as trapping agents.[32–34]

3 Results and discussion

3.1. Two-step pyrolysis synthesis mechanism

Pure and Y/g-C_3N_4 is synthesized by a two-step pyrolysis method, and the possible formation mechanism is given in Scheme 1. Initially, two molecules of urea undergo thermal condensation, resulting in the elimination of NH_3.[35] At 240 °C, urea is converted into melamine *via* a nucleophilic addition condensation reaction.[36] These intermediate products are then converted to melam by the polymerization of melamine at 390 °C, accompanied by the elimination of NH_3.[35,37] Melem is then cooled to room temperature to ensure thermal stability and then calcined again at 550 °C, resulting in the formation of Y/g-C_3N_4.[37,38]

3.2. Structural characterization

FTIR spectra of pure and yttrium-doped g-C_3N_4 are shown in Fig. 1(a and b). g-C_3N_4 exhibits a sharp absorption peak at 810 cm^{-1}, corresponding to the condensed aromatic CN (tri-*s*-triazine units). A strong absorption peak at 1200–1700 cm^{-1} is attributed to the stretching vibration of aromatic heterocyclic ring units (hexazine structure, C–N, C=N).[39,40] Broad peaks between 3000 and 3400 cm^{-1} are assigned to N–H (–NH_2 or =NH) group stretching modes and surface hydroxyl groups (OH).[41] Similarly, Y/g-C_3N_4 shows a similar peak pattern with slight shifts, which may be due to the effect of transition metal doping within the g-C_3N_4 network. However, yttrium doping does not affect the basic chemical structure of g-C_3N_4, and the tri-*s*-triazine peak position is slightly shifted.[41] No distinct yttrium-related peaks are observed during doping due to the low Y-content in these samples.

Fig. 1(c and d) demonstrates the XRD patterns of g-C_3N_4 and Y/g-C_3N_4. Two peaks at 27.50° and 13.26° correspond to the tri-*s*-triazine units of g-C_3N_4, commonly indexed as the (002) and (100) planes of g-C_3N_4, respectively (JCPDS no. 87-1526).[42] XRD results of Y/g-C_3N_4 showed no significant changes. However, as

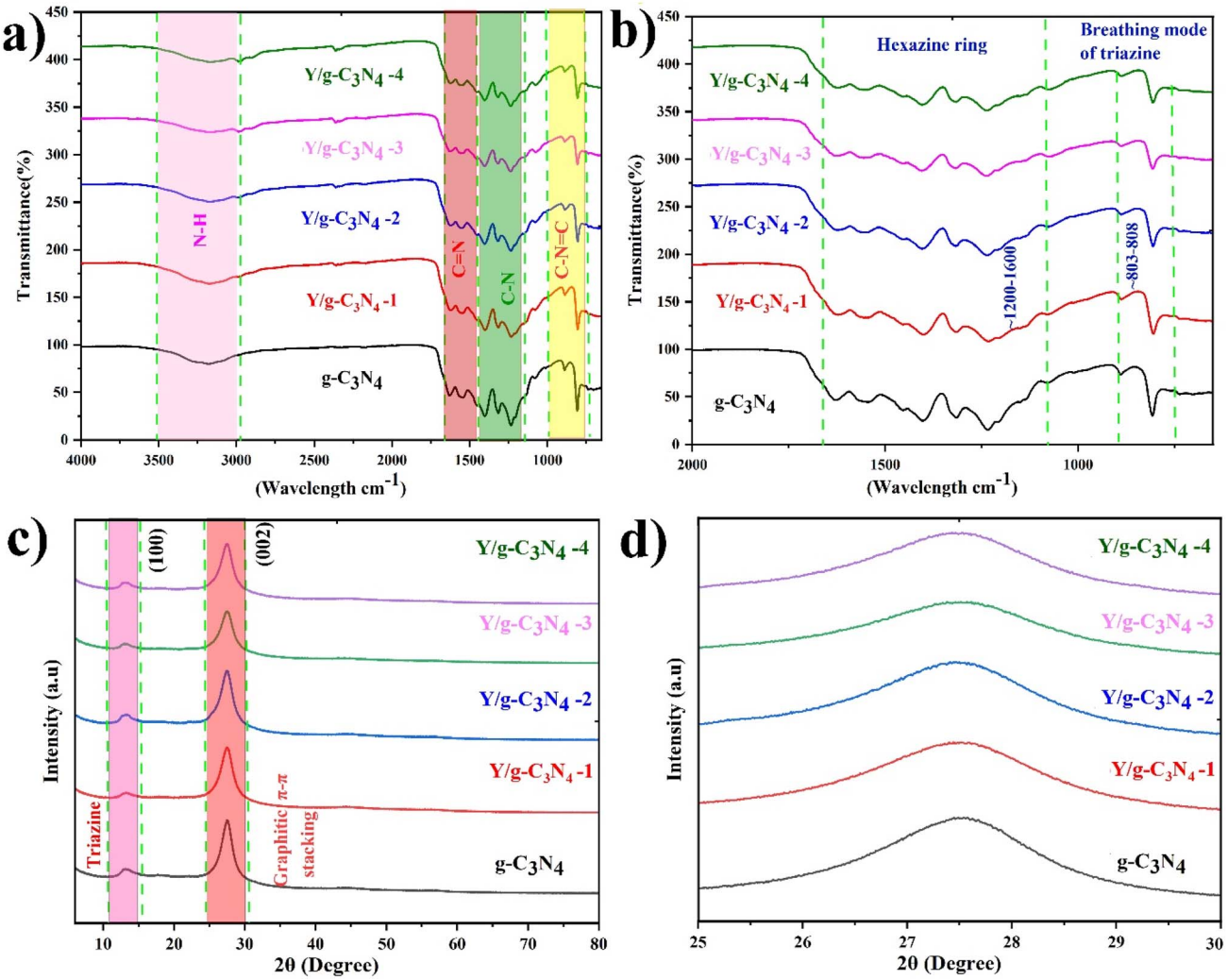

Fig. 1 FTIR (a and b) and XRD (c and d) spectra of pristine and Y/g-C_3N_4.

the doping amount increases, the peak width and intensity decrease, and a slight shift in the peak position occurs. This indicates that the crystal growth of g-C_3N_4 is hindered by doping.[43] This XRD pattern suggests that Y-doping does not affect the basic structure of g-C_3N_4.

Fig. 2(a) displays the N_2 adsorption–desorption isotherms of g-C_3N_4 and Y/g-C_3N_4-3, which reveal type-IV isotherms with H_3-type hysteresis loops characteristic of mesoporous materials. Notably, Y/g-C_3N_4-3 exhibited a significantly higher nitrogen uptake compared to g-C_3N_4, reflecting a substantial increase in specific surface area and pore volume. This is because yttrium metal doping disrupts the orderly growth of g-C_3N_4, resulting in reduced crystallinity and increased structural disorder, producing a loosely packed porous structure with improved surface exposure. The increased surface area suggests the formation of more active sites on Y/g-C_3N_4-3, which enhances photocatalytic efficiency by improving the adsorption, desorption, and diffusion of reactant molecules.[44–49] Fig. 2(b) shows the pore size distribution curves of g-C_3N_4 and Y/g-C_3N_4-3, confirming the mesoporous nature of both materials, with pore diameters distributed below 20 nm. Y/g-C_3N_4-3 shows a slightly broader pore size distribution and wider mesoporous structure compared to g-C_3N_4, which can enhance the diffusion of reactants and be beneficial for catalysis applications. Table S1 provides a detailed description of the textural properties of g-C_3N_4 and Y/g-C_3N_4-3.

TGA and DSC results of synthesized materials are shown in Fig. 3(a–c). g-C_3N_4 is thermally stable below 500 °C, presenting only small changes due to its heterocyclic ring-conjugated system. These heterocyclic rings are connected through C–N bonds, forming a layered structure similar to that of graphite with strong van der Waals forces between layers. With increasing temperature, g-C_3N_4 exhibits higher weight loss due to the weakening intermolecular forces. At 615.83 °C, g-C_3N_4 shows more than 50% weight loss; at 685.71 °C, the weight loss reaches 96–99% (nearly complete decomposition), and below 750 °C, it is completely decomposed. TGA graph of Y/g-C_3N_4 materials is shown in Fig. 3(b and c). By increasing the amount of Y-doping, the thermal stability also improved. DSC analysis is also performed to examine the heat flow into or out of g-C_3N_4

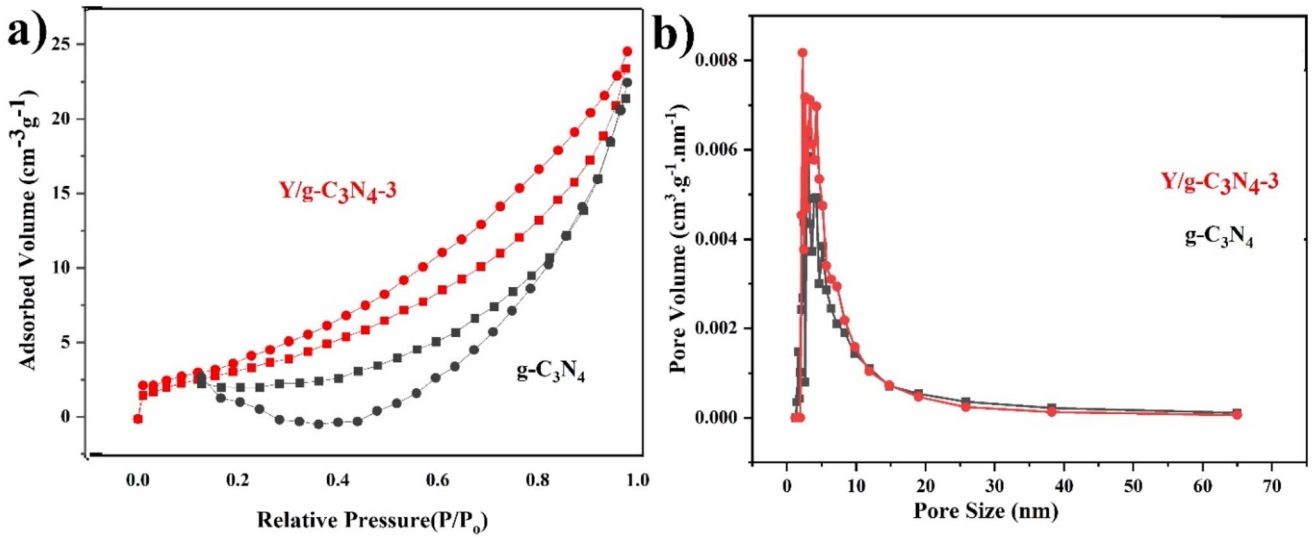

Fig. 2 N_2 adsorption–desorption isotherms (a) and pore size distribution curves of pristine and Y/g-C_3N_4-3 (b).

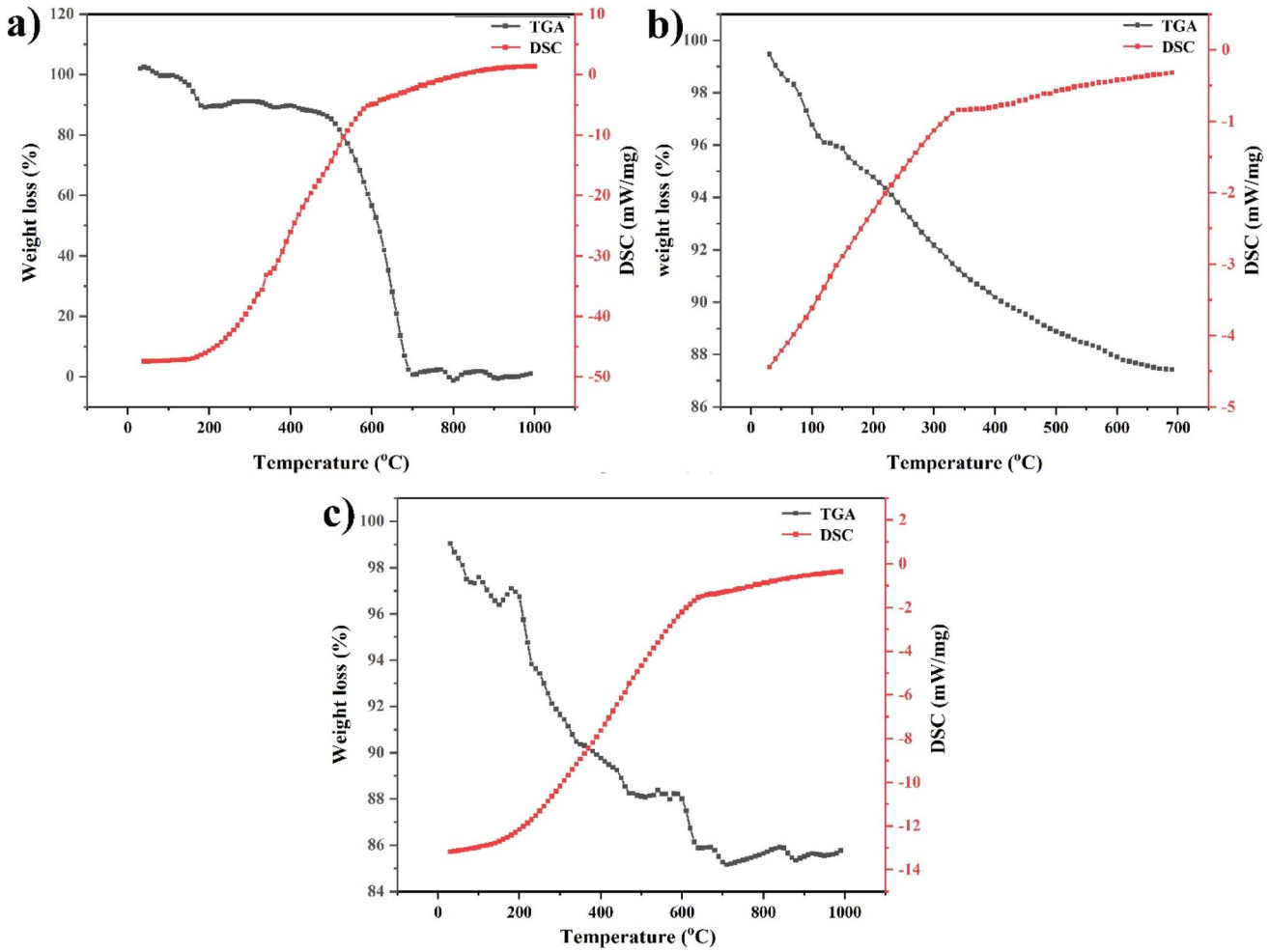

Fig. 3 TGA and DSC curve of pristine g-C_3N_4 (a), Y/g-C_3N_4-1 (b), and Y/g-C_3N_4 (c).

and Y/g-C_3N_4, as shown in Fig. 3(a–c). In pristine g-C_3N_4, a gradual heat absorption is observed at lower temperatures, reflecting its internal thermal stability (Fig. 3(a)). At elevated temperatures, a strong exothermic peak appears, corresponding to the complete decomposition of the material. In contrast, Y/g-C_3N_4 materials display multiple transitions across different temperature ranges as shown in Fig. 3(b and c). These observations suggest that the Y/g-C_3N_4 materials exhibit enhanced thermal stability compared to pristine g-C_3N_4.

3.3. Optical properties of materials

Optical property results of g-C_3N_4 and Y/g-C_3N_4 are presented in Fig. 4(a and b). Fig. 4(a) shows a noticeable red shift and enhanced absorption in Y/g-C_3N_4 in the visible region compared to g-C_3N_4. This red shift becomes more prominent as the concentration of Y-dopant increases. This enhancement is attributed to the incorporation of Y^{3+} ions, which facilitates the d–d transition between Y^{3+} and the conduction band of g-C_3N_4. This interaction leads to improved visible light absorption, making Y/g-C_3N_4-3 a suitable material for photocatalysis. Fig. 4(b) shows the transmittance results of synthesized materials. Y/g-C_3N_4-3 exhibits the lowest transmittance in the visible region compared to g-C_3N_4, further supporting the UV-visible results. The band gap of these materials is also calculated and results are shown in Fig. S1. g-C_3N_4 has a band gap of 2.803 eV, which agrees well with previous literature.[32,50] The band gap of Y/g-C_3N_4-3 decreased to 2.639 eV due to yttrium doping, which enhances low-energy photon utilization through improved interaction with the g-C_3N_4 structure. This interaction causes a negative correction to the conduction band energy and a positive correction to the valence band energy. The narrowing of the bandgap is advantageous for solar light absorption.[33,51]

PL results reflect the transition and recombination of photoinduced charge carriers (Fig. 4(c) and (d)). The PL curve exhibits broad luminescence peaks between 400 and 500 nm at an excitation wavelength of 390 nm. The PL peak intensity of Y/g-C_3N_4 is dramatically reduced compared to that of g-C_3N_4 due to the Y–N bond, which serves as a trap site for photogenerated electrons, effectively hindering the recombination of photogenerated charge carriers. Y/g-C_3N_4-3 has the lowest peak intensity among all yttrium-doped materials, indicating a slower recombination rate of photo-excited electron–hole (e^-/h^+) pairs.[32,52] The suppression effect on photogenerated carriers is lower in Y/g-C_3N_4-1 and Y/g-C_3N_4-2 due to lower Y-content and the small number of Y–N trapping sites. Similarly, the higher amount of Y functions as a recombination center, promoting the recombination of e^-/h^+ pairs.[52] The CIE (1976) chromaticity coordinates of pure and Y/g-C_3N_4-3, calculated using CIE software, are presented in Fig. 4(e). All coordinates fall within the near white light region.

3.4. Morphology and chemical composition study

The topological analysis of g-C_3N_4 and Y/g-C_3N_4 is carried out using AFM (Fig. S2(a–e)). g-C_3N_4 shows larger bulk layers, whereas the Y/g-C_3N_4 materials exhibited noticeable changes in surface topology. In Y/g-C_3N_4-3, the increased roughness compared to other doped materials enhances the specific surface area, improving photocatalytic degradation.[53]

SEM images of g-C_3N_4 and Y/g-C_3N_4 are shown in Fig. 5(a–j). Pristine g-C_3N_4 has a sheet-like (nano-layered) structure. The main reasons reported behind the sheet-like structure of g-C_3N_4 is the use of the precursor urea, which provides a lamellar structure due to the release of NH_3 and CO_2 gases (Fig. 5(a and b)). After doping, the Y-metal alters the physical structure of g-C_3N_4 by softening and loosening the nanolayer packing, confirming the Y doping as shown in Fig. 5(c–j). EDX analysis with elemental mapping is also performed to determine the elemental composition. The EDX analysis and elemental mapping of g-C_3N_4 and Y/g-C_3N_4-3 are presented in Fig. S3 and S4 and Table S2. It is evident that Y-metal is absent in pristine g-C_3N_4, while the doped materials contain Y-metal, indicating a successful doping.

3.5. Charge separation efficiency

Dynamic light scattering (DLS) is utilized to measure the charge on photocatalyst materials, as shown in Fig. S5(a–d). Fig. S5(a) shows a negative charge potential for g-C_3N_4, while Y/g-C_3N_4 materials contained positive charge. The negative charge potential on g-C_3N_4 (−18.4 mV) is consistent with previous literature.[54–56] After doping with Y, the doped materials attained a positive charge on their surface—the net zeta potential on Y/g-C_3N_4.-1 (13 mV), Y/g-C_3N_4-2 (17.2 mV), Y/g-C_3N_4-3 (13.9 mV), and Y/g-C_3N_4-4 (9.94 mV). This type of behavior has been previously reported, in which g-C_3N_4 acquires a positive surface charge after metal doping.[57] Similarly, in Fig. S5(b) and (c), the phase plots (phase = frequency × time) show the difference in phase between the measured beat frequency and a reference frequency as a function of time. The reference frequency is set at 320 Hz. The observed frequency shifts are as follows: g-C_3N_4 at 300 Hz, Y/g-C_3N_4-1 at 323 Hz, Y/g-C_3N_4-2 at 338 Hz, Y/g-C_3N_4-3 at 334 Hz, and Y/g-C_3N_4-4 at 328 Hz. In terms of phase response, g-C_3N_4 exhibited mobility in the negative phase, while all Y/g-C_3N_4 samples showed mobility in the positive phase. Fig. S5(d) shows the Zeta potential current *versus* voltage (for the applied voltage and the current detected in the cell) for the materials. Y-doped photocatalyst exhibited a more pronounced response in applied voltage and current detection compared to the pristine material (likely due to the more electropositive nature of the yttrium metal). These results indicate a clear change in charge separation within g-C_3N_4, which is further enhanced after Y-metal doping, thereby improving its properties.

Additionally, the Zeta size of materials is also measured (Fig. S6). The particle size of g-C_3N_4 is significantly affected by aggregation after surface modification with Y. Zeta size results suggest that g-C_3N_4 has a smaller size which increases with increasing doping amounts. The increase in size is attributed to the Y doping, which involves coordination with water molecules around the Y-metal, increasing the hydrodynamic diameter. Fig. S7 shows the correlation of g-C_3N_4 and Y/g-C_3N_4 materials to evaluate the particle sedimentation with time. All materials sediment over time, and this process affects the size and density of the photocatalyst.

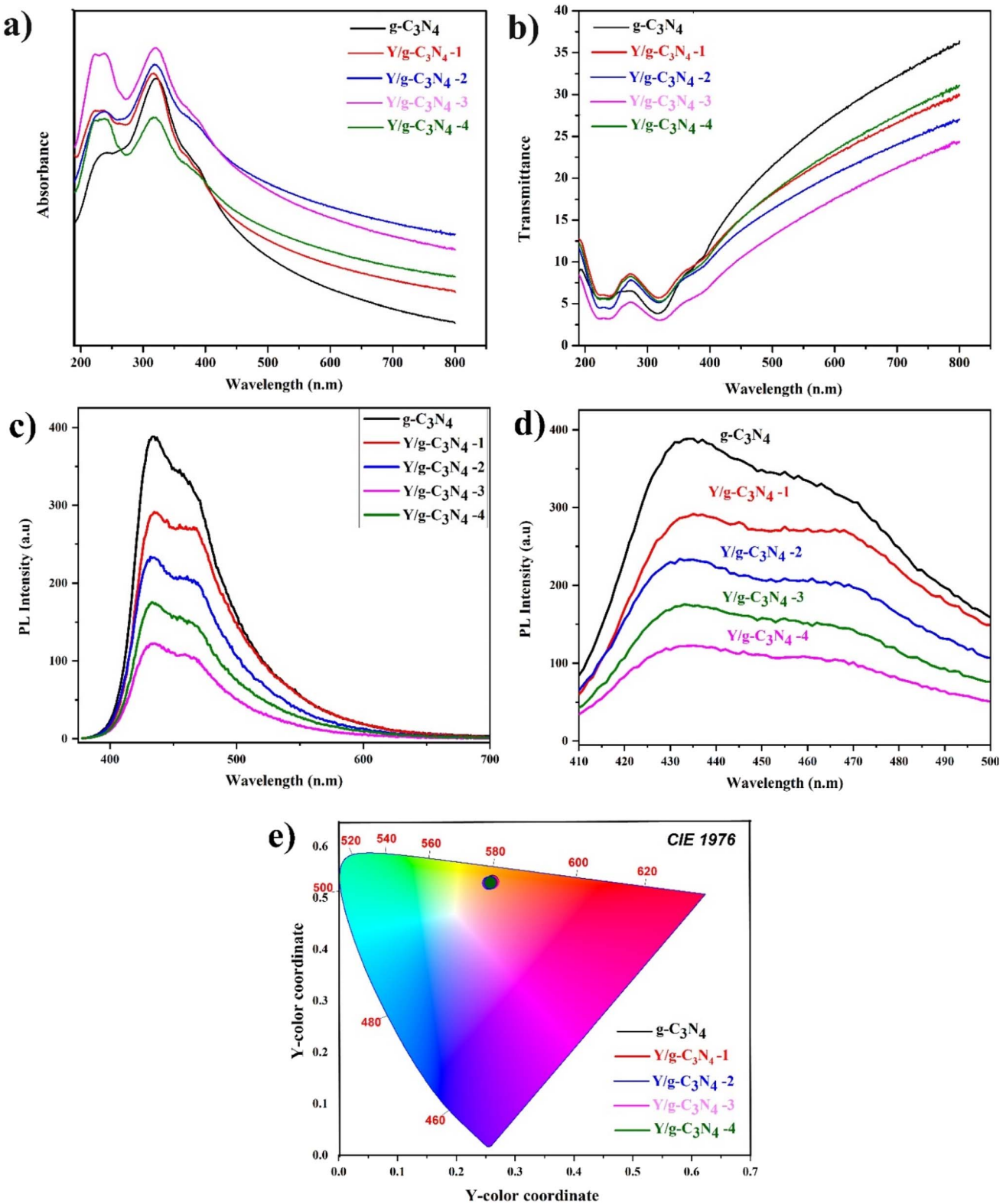

Fig. 4 UV-vis absorption (a), transmittance (b), photoluminescence (c and d), and CIE (1976) chromaticity coordinate (e) of g-C_3N_4 and Y/g-C_3N_4.

3.6. Photocatalytic activity of the prepared catalysts

3.6.1. Methylene blue stability. Before starting the degradation experiment, a blank test is conducted to verify the direct photolysis of MB under visible light irradiation. Fig. S8(a and b) shows the UV-visible and Zeta potential (−9.16 mV) results of MB after 2 h and 4 h of irradiation without using a catalyst. After exposure to light, there is no change in the UV-visible and zeta

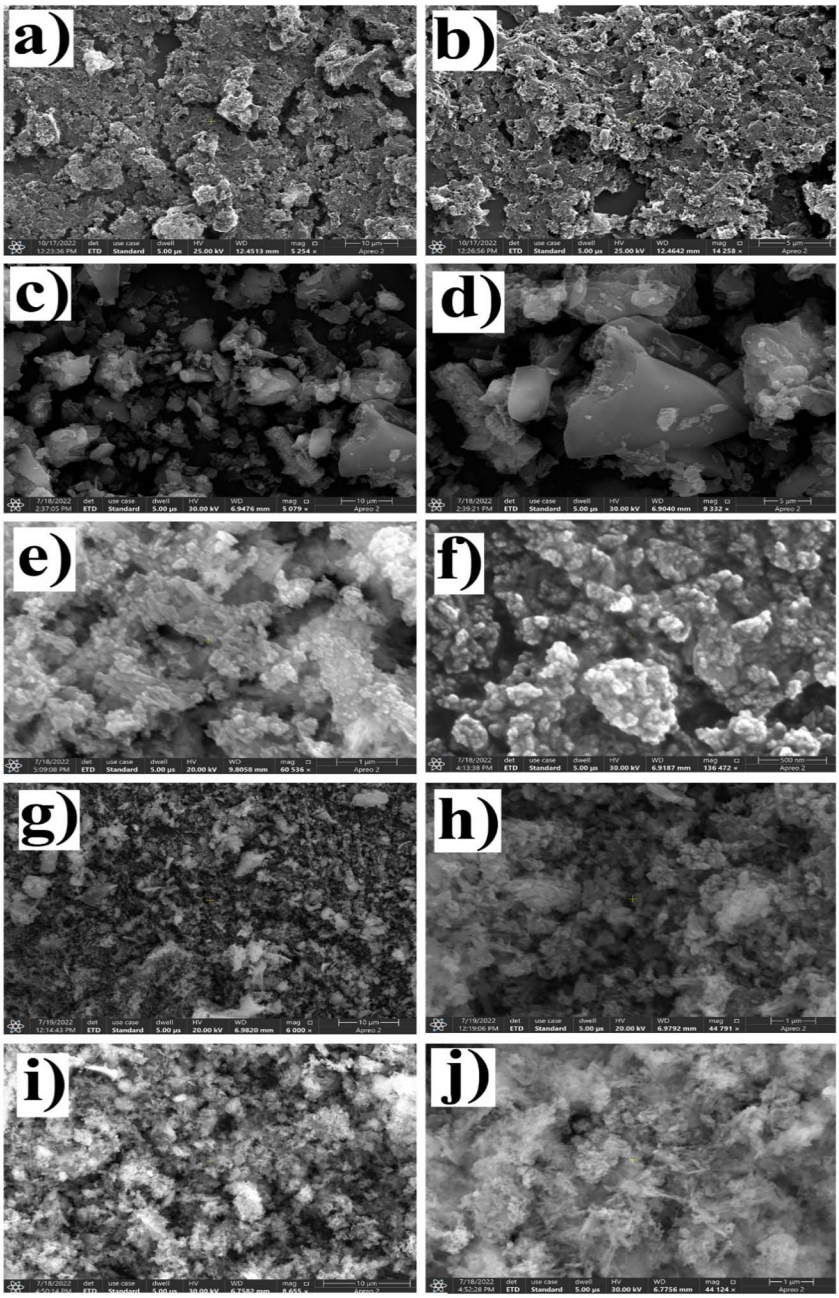

Fig. 5 SEM images of g-C_3N_4 (a and b), Y/g-C_3N_4-1 (c and d), Y/g-C_3N_4-2 (e and f), Y/g-C_3N_4-3 (g and h), and Y/g-C_3N_4-4 (i and j).

potential results, indicating stability of MB. The Zeta potential values of g-C_3N_4, Y/g-C_3N_4-1, Y/g-C_3N_4-2, Y/g-C_3N_4-3, Y/g-C_3N_4-4, and MB are −18.4 mV, 13 mV, 17.2 mV, 13.9 mV, 9.94 mV, and −9.16 mV, respectively (Fig. S9). These results show that the surface charge of Y/g-C_3N_4 materials is more positive than that of pure g-C_3N. This finding indicates that Y/g-C_3N_4 has a superior surface adsorptive ability for MB dyes compared to g-C_3N_4.

3.6.2. Photocatalytic activity. Photodegradation efficiency of g-C_3N_4, Y/g-C_3N_4-1, Y/g-C_3N_4-2, Y/g-C_3N_4-3, and Y/g-C_3N_4-4 is evaluated using standard MB dye ($\lambda_{max} = 664$ nm) under visible light irradiation. All these materials successfully degraded MB, while Y/g-C_3N_4-3 showed the highest degradation efficiency. The photocatalytic activity of g-C_3N is the lowest due to the fast recombination of e^-/h^+ pairs. The experimental calculation results (C/C_0, Langmuir–Hinshelwood model, tap water experiments, and TOC), as shown in Fig. 6(a–d).[8,58,59] Fig. 6(a) illustrates the photocatalytic efficiency (C/C_0) of MB for g-C_3N_4 and Y/g-C_3N_4. Under light irradiation (40 minutes), all samples exhibited time-dependent enhancement in degradation performance. Pristine g-C_3N_4 removed only 68% of MB, whereas Y-doping improved the photocatalytic efficiency. Among the composites, Y/g-C_3N_4-3 demonstrated the highest degradation performance (99%). However, a slight drop in efficiency is observed in Y/g-C_3N_4-4, suggesting that excessive doping may hinder performance by increasing charge recombination. The kinetic model is also applied, and Fig. 6(b) shows the pseudo-

first-order kinetics for MB degradation. The rate constant (k) increased with Y-doping (indicating faster degradation of MB). Pristine g-C_3N_4 showed the lowest rate constant (k = 0.0322 min^{-1}), while Y/g-C_3N_4-3 exhibited the highest rate constant (k = 0.0439 min^{-1}), confirming that Y/g-C_3N_4-3 is the most suitable photocatalyst (Table S3). This trend highlights the role of Y doping in enhancing charge separation and visible light utilization for effective photocatalytic degradation. Other factors included a narrow band gap and hierarchical porosity, allowing more efficient light harvesting. Fig. 6(c) illustrates the degradation of MB in tap water using g-C_3N_4 and Y/g-C_3N_4. All Y-doped samples showed better degradation, as compared to g-C_3N_4. Among them, Y/g-C_3N_4-3 maintained the highest degradation efficiency, proving its strong stability and effectiveness under real water conditions. All catalysts showed reduced degradation in tap water compared to distilled water. This decrease is primarily due to the presence of ions, organic matter, and other impurities. In tap water, interefering species can bind to active sites of the catalyst, scatter light, or quench reactive species, reducing the overall photocatalytic performance. Fig. 6(d) illustrates the total organic carbon (TOC) removal efficiency of g-C_3N_4 and Y/g-C_3N_4 photocatalysts, reflecting the mineralization of MB. Pristine g-C_3N_4 showed the lowest TOC removal, while Y/g-C_3N_4 displayed more mineralization, especially Y/g-C_3N_4-3, confirming their superior ability to mineralize the MB. These results demonstrate that yttrium doping not only accelerates dye decolorization but also enhances full mineralization, making the catalysts more effective for environmental applications.

3.6.3. LC-MS analysis. The proposed degradation mechanism of MB is examined based on the m/z values obtained from LC-MS analysis. LC-MS results of pure and degraded MB are shown in Fig. 7(a–c). An m/z value of 284 confirmed that MB is pure, as shown in Fig. 7(a). When MB is dissolved in water, the S–Cl moiety cleaves from MB due to the water's hydration energy, which indicates the lowest bond dissociation energy.[60] Therefore, the m/z value of 284 is obtained instead of 319.85. Furthermore, Fig. 7(b) and (c) show the degraded products of MB at different time intervals using the Y/g-C_3N_4-3 catalyst. Several peaks are observed with different m/z values (m/z 272, 226, 221, 202, 164, 111, 97, *etc.*). These peaks are attributed to the degradation of MB, with some unpredictable peaks occurring at higher mass

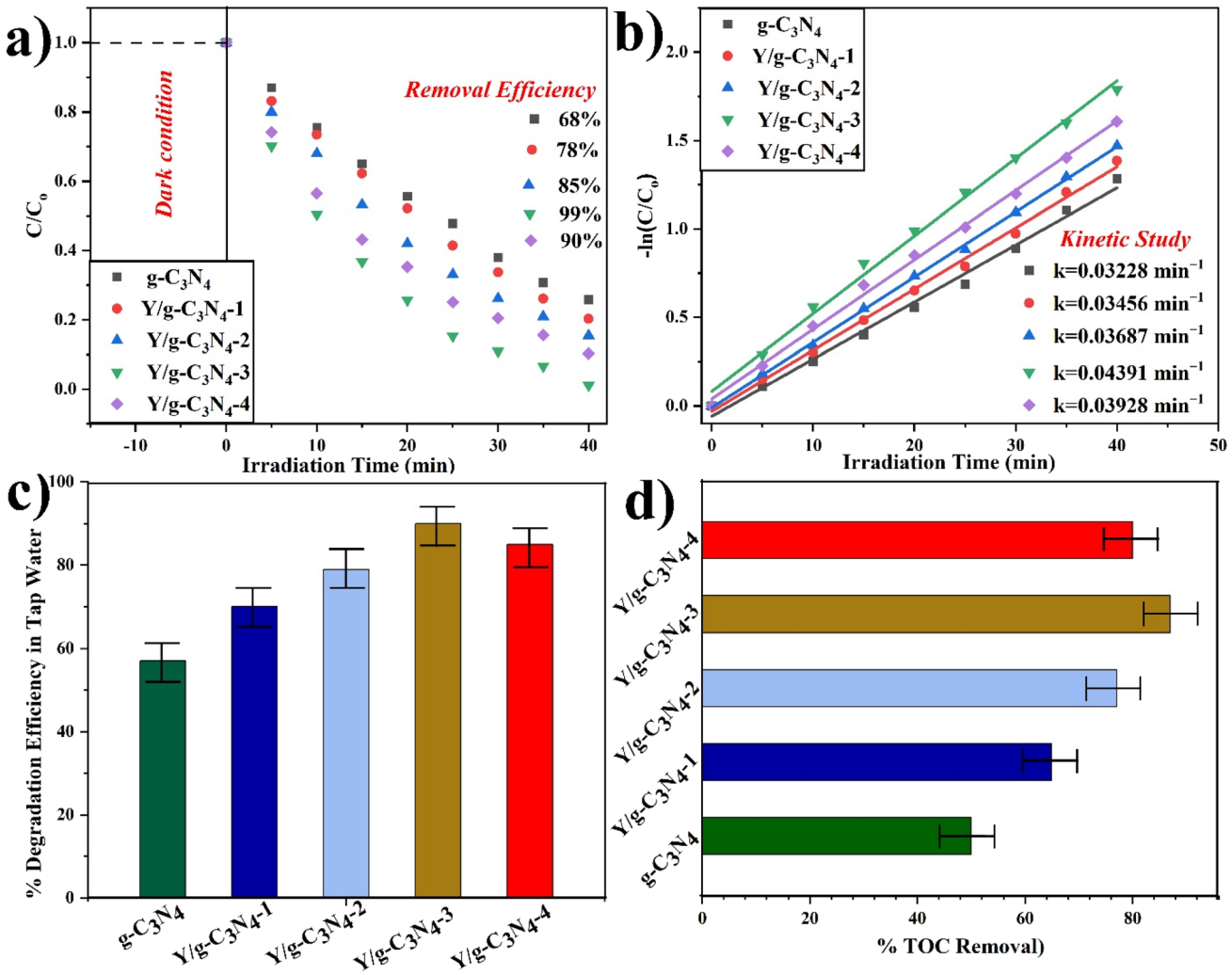

Fig. 6 Photocatalytic degradation efficiency (C/C_0) (a), pseudo-first-order kinetics (b), degradation in tap water (c), and TOC removal of MB (d) using g-C_3N_4 and Y/g-C_3N_4.

than the original mass. The small, low-intensity peaks indicate the presence of low-molecular-weight fragments, suggesting that MB is completely degraded over time.

3.7. Mechanism of the degradation pathway of MB

The photocatalytic degradation of MB starts with the removal of methyl (CH_3) groups (path A) by demethylation, converting MB ($m/z = 319$) into a smaller fragment ($m/z = 294$). An alternative degradation route (path B) involves demethylation (CH_3) to $m/z = 284$ (removing chloride ions), followed by cleavage of the thiazine ring (path B-1). This breakdown produces a series of intermediates with m/z values of 288, 202, 164, and 97. In a parallel route (path B-2), structural changes yield aromatic amine-based by-products with m/z values of 221, 226. Another product is also de-aminated from (B-1A) molecules. The continued fragmentation leads to the formation of simple end products, such as water and CO_2, confirming that MB undergoes complete mineralization through demethylation, ring scission, and molecular breakdown steps (Fig. 8).

3.8. Photocatalytic self-cleaning capability of Y/g-C_3N_4-3 modified cotton fabric

The self-cleaning efficiency of Y/g-C_3N_4-3 photocatalyst is further tested by coating it on cotton fabric. Y/g-C_3N_4-3 coated cotton fabric is tested against the MB stain. Fig. 9(a–f) shows the photocatalytic anti-stain capability of the modified cotton fabric sample in comparison with the pristine cotton fabric. Fig. 9(a and b) shows that due to the hydrophilic nature of pristine cotton, it becomes stained with the MB solution. When this piece of stained cotton fabric is placed under a visible light photoreactor for 1 h, MB did not disappear from the pristine cotton fabric, indicating that pristine cotton does not exhibit self cleaning ability (Fig. 9(c)). Fig. 9(d) shows the cotton fabric after modification with Y/g-C_3N_4-3, which becomes hydrophobic due to the inherent hydrophobic nature of Y/g-C_3N_4-3, preventing MB drops from penetrating inside the cotton surface (Fig. 9(e)). The MB-stained modified cotton fabric sample is also exposed to visible light for 1 h. Due to the photocatalytic properties of Y/g-C_3N_4-3, the MB stain is removed from the surface of the modified cotton fabric (Fig. 9(f). This shows that the designed material can be used as a potential self-cleaning coating agent.

3.9. Charge separation and photocatalytic mechanism

Electrochemical impedance spectroscopy (EIS) is employed to investigate the charge transfer resistance. Fig. S10 shows the Nyquist plots obtained from EIS of both g-C_3N_4 and Y/g-C_3N_4-3. The smaller semicircular arc for Y/g-C_3N_4-3 suggests a lower charge-transfer resistance, reflecting improved electrical conductivity and more efficient charge carrier movement at the

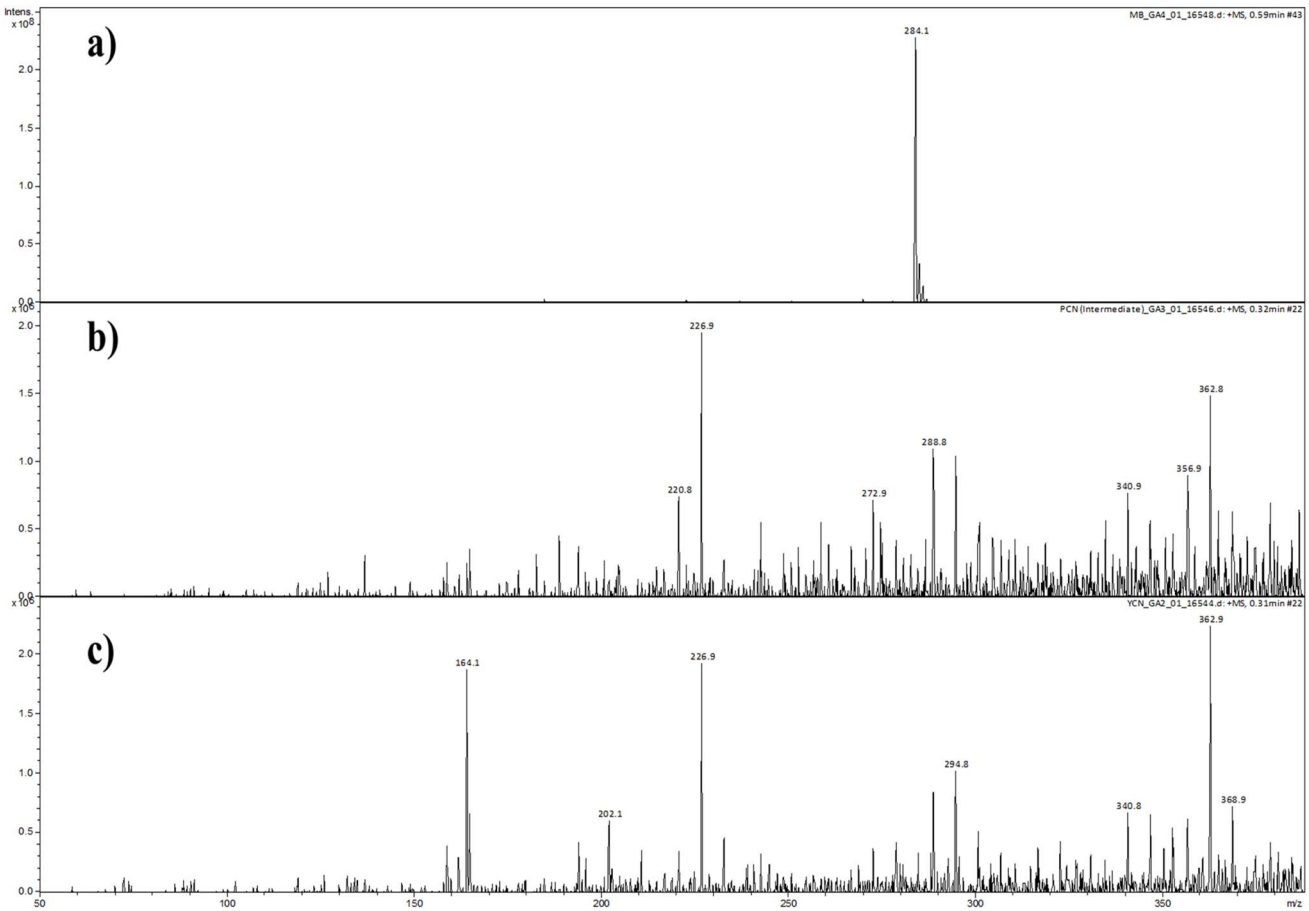

Fig. 7 LC-MS chromatogram of pure MB (a), and degraded products after 24 and 32 minutes using Y/g-C_3N_4-3 (b and c).

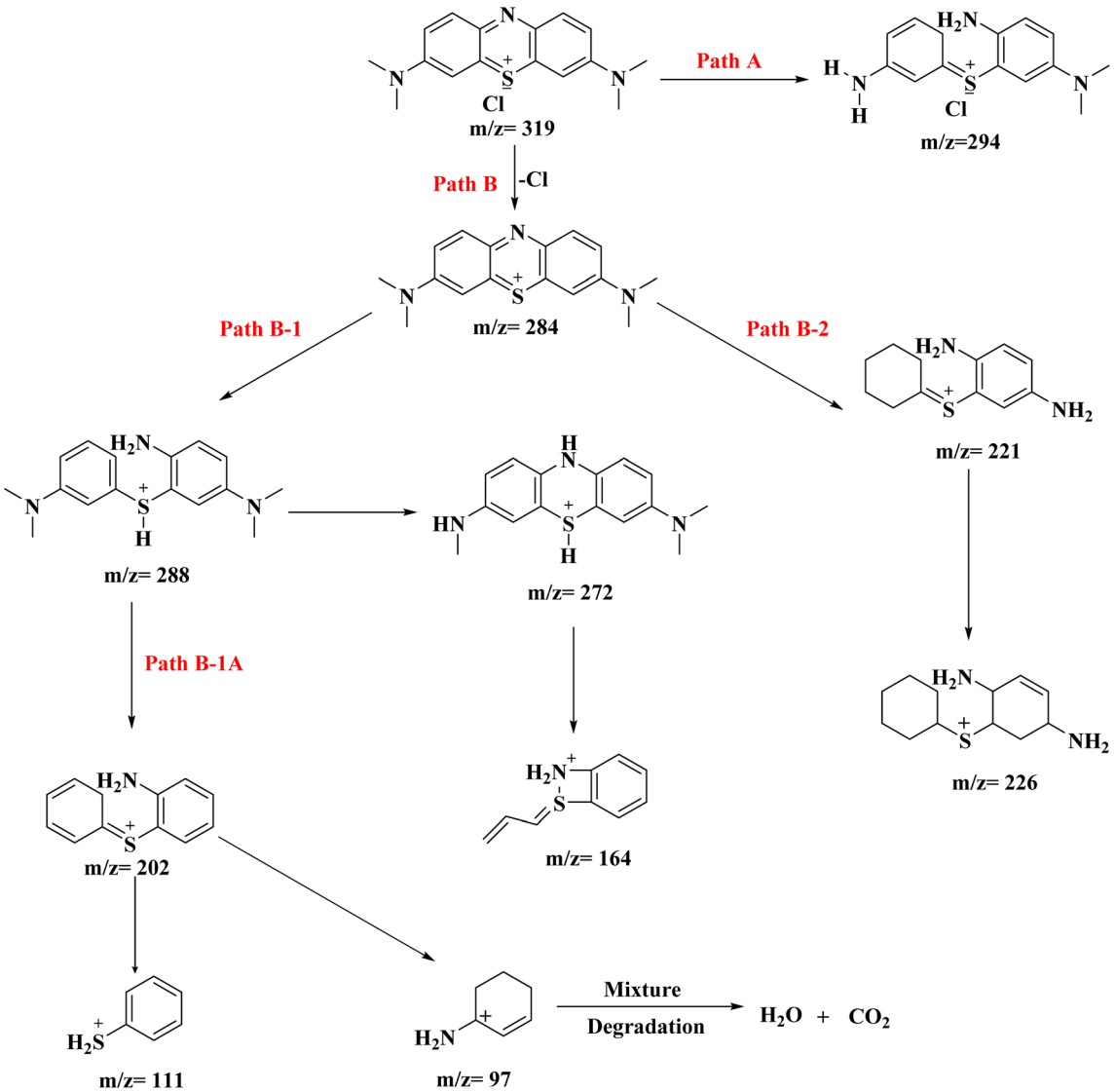

Fig. 8 Mechanism of the breakdown of MB based on the *m/z* value of LC-MS.

interface. Lower resistance implies that electrons can migrate more freely, reducing recombination and improving photocatalytic activity. The inset shows a PL graph, where g-C_3N_4 displays strong emission intensity (indicating a higher recombination rate of photogenerated carriers). At the same time, Y/g-C_3N_4-3 exhibits weaker PL intensity (implying that the incorporation of yttrium effectively reduces carrier recombination). Similarly, Fig. 10(a) presents a schematic diagram of the band structure of g-C_3N_4, while Fig. 10(b) shows that g-C_3N_4-3 and Y/g-C_3N_4-3 have a band gap of 2.803 eV and 2.639 eV, respectively. The reduced band gap facilitates more efficient absorption of visible light. This figure also shows that in the presence of Y enhanced charge separation and inhibited recombination, allowing effective electrons migration for superior photocatalytic performance under visible light.[32] The combined evidence from EIS, PL analysis, and band structure diagrams confirms that Y-doping significantly improves photocatalytic efficiency by enhancing charge separation and reducing resistive losses.

3.10. Trapping agents

Fig. 11(a) shows the effect of different trapping agents on MB photodegradation using Y/g-C_3N_4-3 under visible light. These data show that IPA, BQ, and sodium azide show little impact, indicating that $^{\bullet}OH$, $^{\bullet}O_2^-$, and $^1O_2^-$ play minor roles. On the other hand, the degradation rate is suppressed with the addition of EDTA, implying that holes (h^+) are the main ROS responsible for the degradation of MB.

3.11. Stability and reusability evaluation

The evaluation of photocatalyst stability and reusability is an important factor for real-world applications. MB degradation efficiency (C/C_0) is repeatedly tested using Y/g-C_3N_4-3 under same conditions (Fig. 11(b)). The stability and reusability

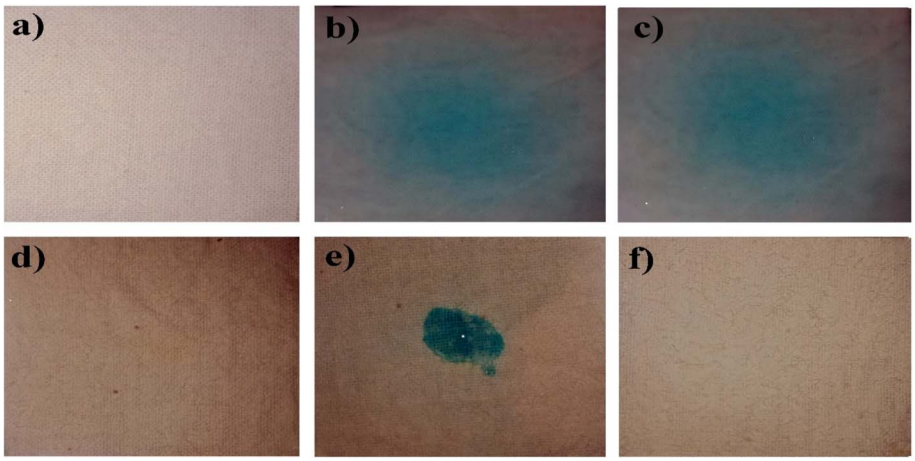

Fig. 9 Photocatalytic self-cleaning characteristics of pristine and modified cotton fabric with Y/g-C_3N_4-3. Pristine cotton fabric (a), stained with MB (b) after 1 h irradiation (c), modified cotton fabric (d), modified cotton stained with MB (e), after 1 h irradiation (f).

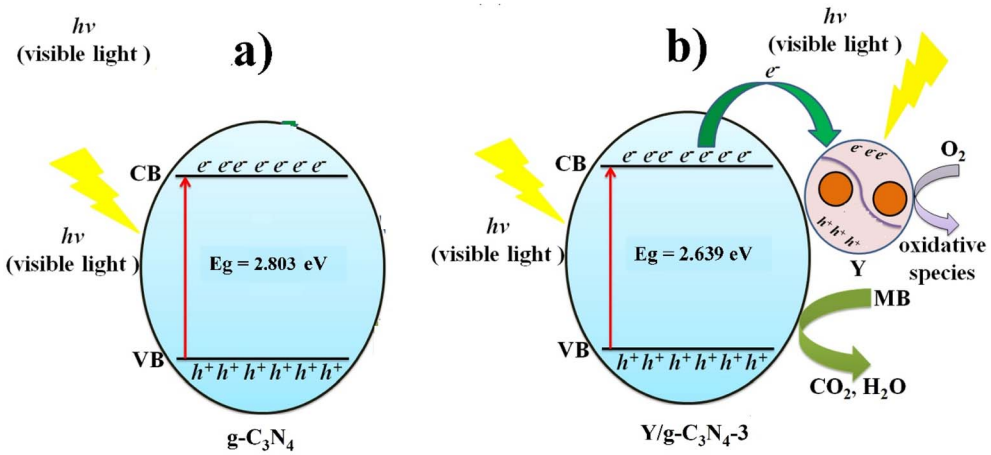

Fig. 10 Schematic illustration of band structure of g-C_3N_4 and Y/g-C_3N_4-3 under visible light for MB degradation (a and b).

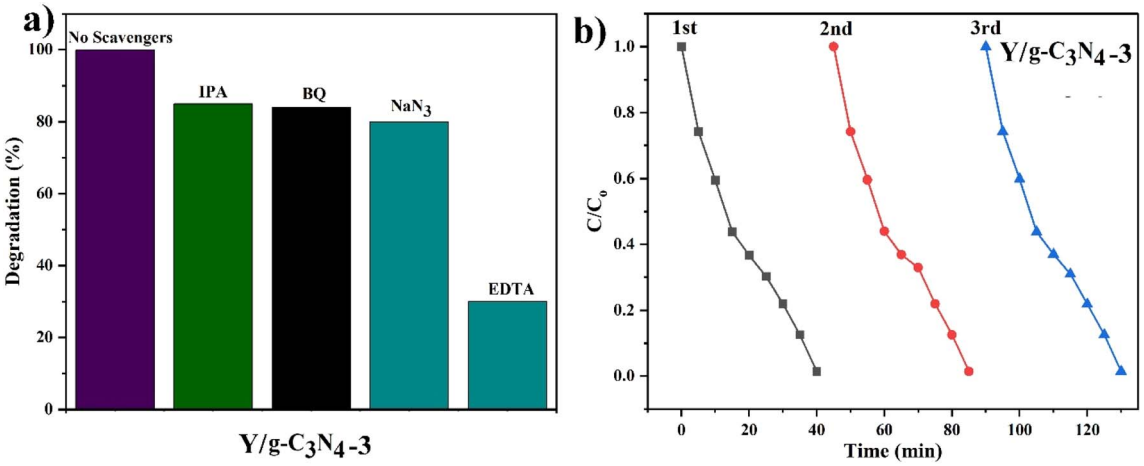

Fig. 11 Effects of various trapping agents on MB photodegradation (a) and Reuseability (b) results of Y/g-C_3N_4-3.

Table 1 Comparison of the previously reported photodegradation efficiency with the current study

No.	Photocatalyst	Source of light	Synthesis method	Organic pollutant	Irradiation time (min)	% degradation	Ref.
1	Ag-doped g-C_3N_4	Xe lamp	Single-step pyrolysis	MB	120	96	61
2	Zr/g-C_3N_4	Xe lamp	Single-step pyrolysis	RhB	110	100	62
3	Co-doped g-C_3N_4	Visible light	Single-step pyrolysis	Eosin B	130	96	46
5	Ti-doped g-C_3N_4	Xenon lamp	Single-step pyrolysis	RhB	50	100	63
6	MnGZ	Solar light	Co-precipitation method	MB	60	100	64
7	Mn-doped g-C_3N_4	300 W Xe arc lamp	Calcination–refluxing	RhB	60	88.9	65
8	B-doped g-C_3N_4 nanosheets	500 W compact fluorescent lamp	Calcination	MB	324	89%	66
9	Y_2O_3/ZnO	300 W ultra-vitalux lamp	Calcination	Sulfamethazine	180	99%	67
10	Y-doped g-C_3N_4	400 W xenon lamp	2-step pyrolysis method	MB	40	99%	Present work

evaluation is conducted three times, showing no change in photocatalytic activity (before and after use). These experiments suggest that there are no structural changes in the photocatalytic material. For comparison, the degradation efficiency of various doped g-C_3N_4 materials is presented in Table 1. The current yttrium-doped sample exhibits a higher degradation rate in the shortest time.

4 Conclusion

Highly efficient Y/g-C_3N_4 is prepared by a two-step pyrolysis method for MB degradation. Y-metal changed the morphology of g-C_3N_4 by softening and loosening the nanolayer packing. Y-doping (Y/g-C_3N_4-1, Y/g-C_3N_4-2, Y/g-C_3N_4-3, and Y/g-C_3N_4-4) enhanced visible light photocatalytic activity as compared to g-C_3N_4. Among these materials, Y/g-C_3N_4-3 showed the highest degradation (99%) for MB and followed pseudo-first-order kinetics ($k = 0.0439$ min^{-1}, $R^2 = 0.999$, $t_{1/2} = 15.78$ min). The photocatalytic activity of Y/g-C_3N_4-3 is enhanced due to Y-metal doping. The most efficient photocatalytic material (Y/g-C_3N_4-3) is tested in tap water which shows a strong photocatalytic activity of 90%. TOC analysis is also performed, confirming that Y/g-C_3N_4-3 exhibited the highest mineralization efficiency (87%). The Y/g-C_3N_4-3 modified cotton fabric exhibited excellent self-cleaning properties. It successfully removed the MB stain within 1 h. These results demonstrates the potential of Y/g-C_3N_4-3 not only as an efficient photocatalyst but also as a promising candidate for practical self-cleaning applications. The experimental result also show that the main reactive species involved in photocatalysis are holes (h^+) and $^{\bullet}OH$, while $^1O_2$ and $^{\bullet}O_2^-$ play a minor role. The intermediate products of MB are analyzed using LC-MS, and a possible degradation pathway of MB is proposed. This work will enable researchers to investigate rare earth metals as dopants in developing efficient photocatalysts for environmental applications.

Author contributions

Muhammad Ikram Nabeel: performed experiments and wrote the original draft. Naseer Ahmad: methodology and validation. Shan Arif: visualization and validation. Dilshad Hussain: conceptualization and writing the final draft. Syed Ghulam Musharraf: supervision and writing the final draft.

Conflicts of interest

The authors declare that they have no conflict of interest.

Data availability

All the data are included in the manuscript and its supplementary information (SI). Supplementary information: additional figures, tables, and experimental details that support the findings of the main manuscript. See DOI: https://doi.org/10.1039/d5na00600g.

Acknowledgements

The authors acknowledge the support of the Higher Education Commission (HEC) of Pakistan.

References

1 V. Saxena, Water Quality, Air Pollution, and Climate Change: Investigating the Environmental Impacts of Industrialization and Urbanization, *Water, Air, Soil Pollut.*, 2025, **236**(2), 1–40.
2 Y. Ruan, Y. Hu and H. Cheng, Recent Progress in g-C3N4-Based Photocatalysts for Organic Pollutant Degradation: Strategies to Improve Photocatalytic Activity, *Catalysts*, 2025, **15**(2), 148.
3 S. Arif, *et al.*, Enhanced Photocatalytic Activity of Sulfur–Nitrogen Co-Doped TiO2 Nanoparticles Synthesized using Dactylorhiza hatagirea Root Extract, *ChemistrySelect*, 2025, **10**(34), e01568.
4 S. Shoran, *et al.*, Synergistic photocatalysis of VO2-A/g-C3N4 composites for efficient degradation of anionic and cationic dyes: towards a sustainable environmental solution, *Appl. Surf. Sci.*, 2025, **684**, 161852.
5 M. I. Nabeel, *et al.*, Recent advancements in the fabrication and photocatalytic applications of graphitic carbon nitride-tungsten oxide nanocomposites, *Nanoscale Adv.*, 2023, **5**(19), 5214–5255.

6 N. C. Oguanobi, *et al.*, Industrial dye effluent sources, generation, and value-added products, in *Engineered Biocomposites for Dye Adsorption*, Elsevier, 2025, pp. 1–10.
7 A. Srivastava, *et al.*, World of the Dye, in *Research Anthology on Emerging Techniques in Environmental Remediation*, IGI Global Scientific Publishing, 2022, pp. 493–507.
8 M. I. Nabeel, *et al.*, Improved visible light-driven photocatalytic degradation of an industrial dye Acid Orange 7 using metal-free sulfur-doped graphitic carbon nitride, *Environ. Sci.: Nano*, 2023, **10**(10), 2810–2830.
9 N. M. Khan, *et al.*, Prunus armeniaca Assisted Green Synthesis of Fe2O3/NiO Nanohybrids Using Unripened Fruit Extract for Remediation of Acid Orange 7 Dye: A Sustainable Environmental Cleaner Approach, *Waste Biomass Valorization*, 2024, 1–19.
10 O. M. A. Halim, *et al.*, A review on modified ZnO for the effective degradation of methylene blue and rhodamine B, *Results Surf. Interfaces*, 2025, **18**, 100408.
11 W. Ahmad, *et al.*, Silica-based superhydrophobic and superoleophilic cotton fabric with enhanced self-cleaning properties for oil–water separation and methylene blue degradation, *Langmuir*, 2024, **40**(11), 5639–5650.
12 J. Hong, J. Bao and Y. Liu, Removal of Methylene Blue from Simulated Wastewater Based upon Hydrothermal Carbon Activated by Phosphoric Acid, *Water*, 2025, **17**(5), 733.
13 M. I. Nabeel, *et al.*, Facile one-pot synthesis of metal and non-metal doped g-C3N4 photocatalyst for rapid acetaminophen remediation, *Carbon*, 2025, 120472.
14 R. Andreozzi, *et al.*, Advanced oxidation processes (AOP) for water purification and recovery, *Catal. Today*, 1999, **53**(1), 51–59.
15 E. Brillas, A review on the application of single and combined Fenton, photo-Fenton, and electrochemical advanced oxidation processes to remove diclofenac from aqueous media, *J. Environ. Chem. Eng.*, 2025, 115443.
16 O. O. Akerele, *et al.*, Performance assessment of ionization chambers in standard diagnostic radiology beams through the determination of calibration coefficients, *Radiat. Meas.*, 2025, **181**, 107349.
17 A. Zuorro and R. Lavecchia, Evaluation of UV/H2O2 advanced oxidation process (AOP) for the degradation of diazo dye Reactive Green 19 in aqueous solution, *Desalination Water Treat.*, 2014, **52**(7–9), 1571–1577.
18 M. A. Khan, *et al.*, Recent advances over the doped g-C3N4 in photocatalysis: a review, *Coord. Chem. Rev.*, 2025, **522**, 216227.
19 S. Khan, *et al.*, Photocatalytic dye degradation from textile wastewater: a review, *ACS Omega*, 2024, **9**(20), 21751–21767.
20 N. Ahmad, *et al.*, Facile modification of nylon filter via vacuum coating with chitosan@ MCM-41/GO for efficient oily wastewater treatment, *J. Mater. Chem. A*, 2025, **13**, 21993–22008.
21 N. Ahmad, *et al.*, Stearic acid and CeO2 nanoparticles Co-functionalized cotton fabric with enhanced UV-block, self-cleaning, water-repellent, and antibacterial properties, *Langmuir*, 2023, **39**(33), 11571–11581.
22 N. Ahmad, *et al.*, Hierarchically grown CeO2/GO on nylon filter with enhanced hydrophilicity and permeation flux for oil-water separation, *Sustain. Mater. Technol.*, 2023, **37**, e00698.
23 H. M. Tofail, *et al.*, Modified g-C3N4 Photocatalysts for Clean Energy and Environmental Applications: A Review, *Sustain. Energy Fuels*, 2025, **9**, 2900–2927.
24 Y. Wang, *et al.*, Simple synthesis of Zr-doped graphitic carbon nitride towards enhanced photocatalytic performance under simulated solar light irradiation, *Catal. Commun.*, 2015, **72**, 24–28.
25 M. I. Nabeel, *et al.*, Tailoring Graphitic Carbon Nitride (g-C3N4) for Multifunctional Applications: Strategies for Overcoming Challenges in Catalysis and Energy Conversion, *Int. J. Energy Res.*, 2025, **2025**(1), 5599894.
26 J. Jiang, *et al.*, A comparison study of alkali metal-doped g-C3N4 for visible-light photocatalytic hydrogen evolution, *Chin. J. Catal.*, 2017, **38**(12), 1981–1989.
27 B. L. Phoon, *et al.*, Co-doped, tri-doped, and rare-earth-doped g-C3N4 for photocatalytic applications: state-of-the-art, *Catalysts*, 2022, **12**(6), 586.
28 N. Y. Devi, *et al.*, Effect of yttrium doping on enhancing the photocatalytic performance of TiO2/GO nanocomposite, *Opt. Mater.*, 2024, **155**, 115791.
29 D. Dai, *et al.*, Construction of Y-Doped BiVO4 Photocatalysts for Efficient Two-Electron O2 Reduction to H2O2, *Chem.–Eur. J.*, 2023, **29**(25), e202203765.
30 X. Liu, *et al.*, Preparation and photocatalytic activity of Y-doped Bi2O3, *J. Alloys Compd.*, 2015, **651**, 135–142.
31 M. Shkir, *et al.*, Enhanced photocatalytic and antibacterial properties of yttrium-doped tungsten oxide (WO_3) nanorods synthesized via hydrothermal method for environmental remediation, *J. Alloys Compd.*, 2025, **1010**, 177857.
32 W. Zhang, L. Zhou and H. Deng, Ag modified g-C3N4 composites with enhanced visible-light photocatalytic activity for diclofenac degradation, *J. Mol. Catal. A: Chem.*, 2016, **423**, 270–276.
33 L. Wang, *et al.*, Cobalt-doped g-C3N4 as a heterogeneous catalyst for photo-assisted activation of peroxymonosulfate for the degradation of organic contaminants, *Appl. Surf. Sci.*, 2019, **467**, 954–962.
34 V. Shanmugam, *et al.*, Fabrication of heterostructured vanadium modified g-C3N4/TiO2 hybrid photocatalyst for improved photocatalytic performance under visible light exposure and antibacterial activities, *J. Ind. Eng. Chem.*, 2019, **76**, 318–332.
35 Q. Su, *et al.*, Urea-derived graphitic carbon nitride as an efficient heterogeneous catalyst for CO 2 conversion into cyclic carbonates, *Catal. Sci. Technol.*, 2014, **4**(6), 1556–1562.
36 T. K. Mukhopadhyay, L. Leherte and A. Datta, Molecular mechanism for the self-supported synthesis of graphitic carbon nitride from urea pyrolysis, *J. Phys. Chem. Lett.*, 2021, **12**(5), 1396–1406.
37 D. R. Paul, *et al.*, Effect of calcination temperature, pH and catalyst loading on photodegradation efficiency of urea

derived graphitic carbon nitride towards methylene blue dye solution, *RSC Adv.*, 2019, **9**(27), 15381–15391.
38 L. Wang, *et al.*, Graphitic carbon nitride-based photocatalytic materials: preparation strategy and application, *ACS Sustain. Chem. Eng.*, 2020, **8**(43), 16048–16085.
39 C. Li, *et al.*, Insight into photocatalytic activity, universality and mechanism of copper/chlorine surface dual-doped graphitic carbon nitride for degrading various organic pollutants in water, *J. Colloid Interface Sci.*, 2019, **538**, 462–473.
40 R. Ding, *et al.*, Preparation of tellurium doped graphitic carbon nitride and its visible-light photocatalytic performance on nitrogen fixation, *Colloids Surf., A*, 2019, **563**, 263–270.
41 B. Babu, J. Shim and K. Yoo, Efficient solar-light-driven photoelectrochemical water oxidation of one-step in-situ synthesized Co-doped g-C3N4 nanolayers, *Ceram. Int.*, 2020, **46**(10), 16422–16430.
42 F. Fina, *et al.*, Structural investigation of graphitic carbon nitride via XRD and neutron diffraction, *Chem. Mater.*, 2015, **27**(7), 2612–2618.
43 S. Hu, *et al.*, Band gap-tunable potassium doped graphitic carbon nitride with enhanced mineralization ability, *Dalton Trans.*, 2015, **44**(3), 1084–1092.
44 C. Xu, *et al.*, Facile in situ fabrication of Co nanoparticles embedded in 3D N-enriched mesoporous carbon foam electrocatalyst with enhanced activity and stability toward oxygen reduction reaction, *J. Mater. Sci.*, 2019, **54**(7), 5412–5423.
45 B.-W. Sun, *et al.*, In situ synthesis of polymetallic Co-doped g-C3N4 photocatalyst with increased defect sites and superior charge carrier properties, *Carbon*, 2017, **117**, 1–11.
46 D. Das, *et al.*, Effect of cobalt doping into graphitic carbon nitride on photo induced removal of dye from water, *Mater. Res. Bull.*, 2017, **89**, 170–179.
47 Q. Sun, *et al.*, Effect of contact interface between TiO2 and g-C3N4 on the photoreactivity of g-C3N4/TiO2 photocatalyst:(0 0 1) vs (1 0 1) facets of TiO2, *Appl. Catal., B*, 2015, **164**, 420–427.
48 S. Hu, *et al.*, Enhanced visible light photocatalytic performance of g-C3N4 photocatalysts co-doped with iron and phosphorus, *Appl. Surf. Sci.*, 2014, **311**, 164–171.
49 Y. Dou, *et al.*, Highly mesoporous carbon nitride photocatalysts for efficient and stable overall water splitting, *Appl. Surf. Sci.*, 2020, **509**, 144706.
50 S. Yan, Z. Li and Z. Zou, Photodegradation performance of g-C3N4 fabricated by directly heating melamine, *Langmuir*, 2009, **25**(17), 10397–10401.
51 Y. Lee, A. Ramdas and R. Aggarwal, Energy gap, excitonic, and "internal''Mn 2+ optical transition in Mn-based II-VI diluted magnetic semiconductors, *Phys. Rev. B:Condens. Matter Mater. Phys.*, 1988, **38**(15), 10600.
52 X. Yang, *et al.*, In situ synthesis of 2D ultrathin cobalt doped g-C3N4 nanosheets enhances photocatalytic performance by accelerating charge transfer, *J. Alloys Compd.*, 2021, **859**, 157754.
53 Z. Zhu, *et al.*, Insight into the effect of co-doped to the photocatalytic performance and electronic structure of g-C3N4 by first principle, *Appl. Catal., B*, 2019, **241**, 319–328.
54 L. Yang, *et al.*, Enhanced photocatalytic activity of g-C3N4 2D nanosheets through thermal exfoliation using dicyandiamide as precursor, *Ceram. Int.*, 2018, **44**(17), 20613–20619.
55 M. Padervand and S. Hajiahmadi, Ag/AgCl@ tubular g-C3N4 nanostructure as an enhanced visible light photocatalyst for the removal of organic dye compounds and biomedical waste under visible light, *J. Photochem. Photobiol., A*, 2022, **425**, 113700.
56 R. Sankar, *et al.*, Green synthesis of colloidal copper oxide nanoparticles using Carica papaya and its application in photocatalytic dye degradation, *Spectrochim. Acta, Part A*, 2014, **121**, 746–750.
57 P. Praus, *et al.*, Synthesis and properties of nanocomposites of WO3 and exfoliated g-C3N4, *Ceram. Int.*, 2017, **43**(16), 13581–13591.
58 J. Huang, *et al.*, Ultrathin Ag2WO4-coated P-doped g-C3N4 nanosheets with remarkable photocatalytic performance for indomethacin degradation, *J. Hazard Mater.*, 2020, **392**, 122355.
59 K. N. Van, *et al.*, A novel preparation of GaN-ZnO/g-C3N4 photocatalyst for methylene blue degradation, *Chem. Phys. Lett.*, 2021, **763**, 138191.
60 G. A. Ashraf, *et al.*, Mesoporous SnMgNd substituted M-hexaferrite catalyzed heterogeneous photo-Fenton-like activity for degradation of methylene blue, *J. Colloid Interface Sci.*, 2019, **557**, 408–422.
61 D. R. Paul, *et al.*, Silver doped graphitic carbon nitride for the enhanced photocatalytic activity towards organic dyes, *J. Nanosci. Nanotechnol.*, 2019, **19**(8), 5241–5248.
62 Y. Wang, *et al.*, Simple synthesis of Zr-doped graphitic carbon nitride towards enhanced photocatalytic performance under simulated solar light irradiation, *Catal. Commun.*, 2015, **72**, 24–28.
63 Y. Wang, *et al.*, Synthesis of Ti-doped graphitic carbon nitride with improved photocatalytic activity under visible light, *Mater. Lett.*, 2015, **139**, 70–72.
64 M. A. Qamar, *et al.*, Fabrication of g-C3N4/transition metal (Fe, Co, Ni, Mn and Cr)-doped ZnO ternary composites: excellent visible light active photocatalysts for the degradation of organic pollutants from wastewater, *Mater. Res. Bull.*, 2022, **147**, 111630.
65 J.-C. Wang, *et al.*, Porous Mn doped g-C3N4 photocatalysts for enhanced synergetic degradation under visible-light illumination, *J. Hazard Mater.*, 2017, **339**, 43–53.
66 Q. Yan, *et al.*, Facile synthesis and superior photocatalytic and electrocatalytic performances of porous B-doped g-C3N4 nanosheets, *J. Mater. Sci. Technol.*, 2018, **34**(12), 2515–2520.
67 M. Belghiti, *et al.*, Synthesis and characterization of Y2O3 partially coated ZnO for highly efficient photocatalytic degradation of sulfamethazine, *J. Mol. Struct.*, 2022, **1251**, 132036.